Molecular Mechanisms of How Mercury Inhibits Water Permeation through Aquaporin-1: Understanding by Molecular Dynamics Simulation

Yoshinori Hirano,[†‡*] Noriaki Okimoto,[‡] Ikuko Kadohira,[†] Makoto Suematsu,[§] Kenji Yasuoka,[¶] and Masato Yasui[†*]
[†]Department of Pharmacology, School of Medicine, Keio University, Shinjuku-ku, Tokyo, Japan; [‡]Computational Systems Biology Research Group, Advanced Computational Sciences Department High Performance Molecular Simulation team, RIKEN, 61-1 Onocho, Tsurumi-ku, Yokohama-shi, Kanagawa, Japan; [§]Department of Biochemistry and Integrative Medical Biology, School of Medicine, Keio University, Shinjuku-ku, Tokyo, Japan; and [¶]Department of Mechanical Engineering, Science and Technology Keio University, Hiyoshi 3-14-1, Kohoku-ku, Yokohama-shi, Kanagawa, Japan

ABSTRACT Aquaporin (AQP) functions as a water-conducting pore. Mercury inhibits the water permeation through AQP. Although site-directed mutagenesis has shown that mercury binds to Cys^{189} during the inhibition process, it is not fully understood how this inhibits the water permeation through AQP1. We carried out 40 ns molecular dynamics simulations of bovine AQP1 tetramer with mercury (Hg-AQP1) or without mercury (Free AQP1). In Hg-AQP1, Cys^{191} (Cys^{189} in human AQP1) is converted to Cys-SHg^{+} in each monomer. During each last 10 ns, we observed water permeation events occurred 23 times in Free AQP1 and never in Hg-AQP1. Mercury binding did not influence the whole structure, but did induce a collapse in the orientation of several residues at the ar/R region. In Free AQP1, backbone oxygen atoms of Gly^{190}, Cys^{191}, and Gly^{192} lined, and were oriented to, the surface of the water pore channel. In Hg-AQP1, however, the SHg^{+} of Cys191-SHg^{+} was oriented toward the outside of the water pore. As a result, the backbone oxygen atoms of Gly^{190}, Cys^{191}, and Gly^{192} became disorganized and the ar/R region collapsed, thereby obstructing the permeation of water. We suggest that mercury disrupts the water pore of AQP1 through local conformational changes in the ar/R region.

INTRODUCTION

Aquaporin (AQP) functions principally as a water channel, transporting water through biological membranes. In humans, 13 different AQPs (AQP0-12) have been identified, each with a different tissue distribution, with some physiological importance (1,2). AQP is not permeated by ions, particularly protons, and this is critical for the homeostasis of membrane potentials and the intracellular pH. The structure of AQP1 has six transmembrane helices (H1–H6) and two short helices (HB and HE). Two characteristic domains regulate water permeation through AQP1. One domain has two highly conserved Asn-Pro-Ala (NPA) motifs, which are held together in the middle of the membrane layer at the two short helices, HB and HE. The Asn residues of the two NPA motifs are close to each other, and the carbonyl oxygens of their side chains make hydrogen bonds with amide groups of two Asn side chains that orient the channel pore. This orientation allows a water molecule to form hydrogen bonds with two amide groups of the Asn residues at center of the pore. The other domain is an aromatic constriction region (ar/R region), formed by Phe^{58}, His^{182}, Cys^{191}, and Arg^{197} (in bovine AQP1) (3,4). Some studies using molecular dynamics (MD) simulations have suggested the presence of another energy barrier that offers both steric and electrostatic selectivity at the ar/R region. Some AQPs are permeated not only by water, but also by gasses, ions, glycerol, and other small molecules (5–8). In some AQPs, the ar/R region is slightly wider because the His residue is replaced by a Gly residue, which allows glycerol to pass through (9). Therefore, both the Arg and His residues of the ar/R region and the Asn residues of the NPA motifs have desolvating effects.

It is known that mercury inhibits most AQPs, including AQP1, by interacting with cysteine residues (10–12). These residues have been identified as Cys^{189} in human AQP1 and Cys^{191} in bovine AQP1, and they exist at the ar/R region, located 8 Å above the NPA region (Fig. 1 *a*). There are two hypotheses for the mechanism of inhibition of AQP1 by mercury; the first is simple occlusion of the channel pore by the mercury atom, the second is that there is a conformational change at the ar/R region that includes the mercury-sensitive cysteine residue of AQP1. To clarify how mercury inhibits the water conductance of AQP1, we carried out MD simulations. MD simulation is a convenient method used commonly to obtain information regarding the dynamic movements of protein and water molecules. The permeation of water through AQP has been studied previously using theoretical methods (3,13–21) but the inhibitory mechanism by mercury has not yet been clarified. We carry out MD simulations of a bovine AQP1, with and without adding Hg^{2+} to Cys^{191} (or Cys^{152}). We have compared the MD trajectories of Free AQP1 and Hg-AQP1, to clarify how the binding of mercury to Cys^{191} inhibits the permeation of water through AQP1.

Submitted July 27, 2009, and accepted for publication December 22, 2009.

*Correspondence: hirano@riken.jp or myasui@sc.itc.keio.ac.jp

Editor: Gerhard Hummer.

© 2010 by the Biophysical Society

0006-3495/10/04/1512/8 $2.00

doi: 10.1016/j.bpj.2009.12.4310

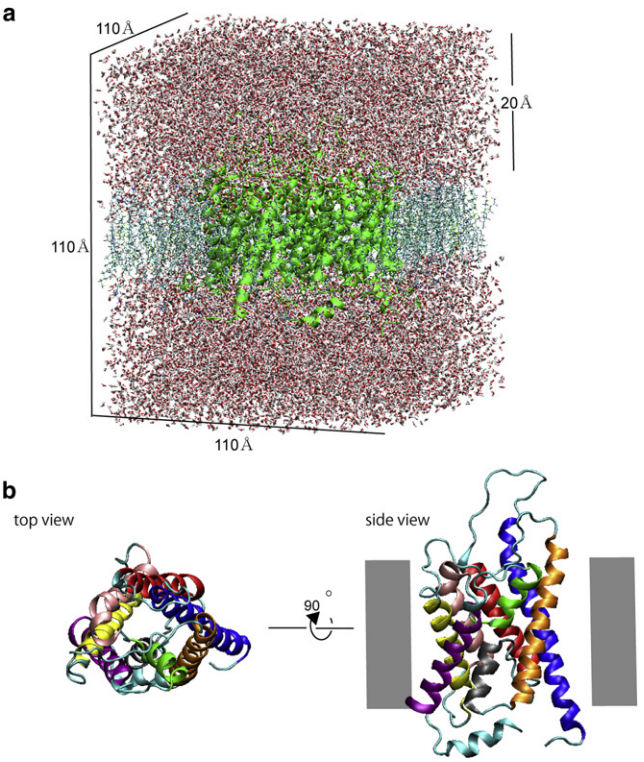

FIGURE 1 (*a*) The simulation system. The size of the initial system is ~110 × 110 × 110 Å^3. The tetramer of AQP1 (*green*), the lipid bilayer (*sky blue*), and water molecules are shown. Water molecules are placed 20 Å from lipid bilayer. (*b*) Top (*left*) and side (*right*) views of the AQP1 monomer. AQP1 consists of six transmembrane helices: H1 (*blue*), H2 (*red*), H3 (*orange*), H4 (*yellow*), H5 (*pink*), and H6 (*purple*); and two short helices: HB (*gray*) and HE (*green*). The gray zone indicates the location of the membrane. The model was drawn using the program VMD (39).

METHODS

MD simulation

To clarify the mechanism of the inhibition of water transport in AQP1 by mercury, we carried out MD simulations of AQP1 in the presence and absence of mercury. The initial system of Free AQP1 was constructed as follows. The initial structure of the homotetrameric assembly of Free AQP1 (based on the x-ray crystallographic structure (22)) was embedded into a 1-palmitoyl-2-oleoyl-phosphatidylethanolamine (POPE) bilayer and then water molecules were added on both sides of the Free AQP1-membrane complex. The size of the initial system was ~110 × 110 × 110 Å^3 (Fig. 1 *b*), and it contained 104,990 atoms (the Free AQP1 protein, 142 POPE lipids and 23,052 water molecules). To remove steric hindrance from the system, we carried out 2 ns of MD simulation, and then used the final structure from this preliminary MD simulation as the initial state of Free AQP1. For the complex of AQP1 with mercury (Hg-AQP1), we constructed the initial structure using the final structure from the MD simulation of Free AQP1. It has been well established that mercury forms a covalent bond with the sulfur atom of Cys^{191}, because site-directed mutagenesis has identified the Cys residue at the ar/R region as the binding site for mercury (10,11), and because the inhibition by mercury can only be reversed by breaking the covalent bond (10). We therefore replaced the Cys^{191} in each monomer by a Cys-SHg$^+$ residue. These two systems, Free AQP1 and Hg-AQP1, were then used for this study.

All MD simulations were carried out using a constant number of molecules, a pressure of 1 atom, and a temperature of 310 K, according to Berendsen's algorithm with a coupling time of 0.2 ps after each system had been heated to 310 K over the first 100 ps. The time step was set at 1 fs. The bond lengths involving the hydrogen atoms were constrained to equilibrium lengths using the SHAKE method. Parm99 and gaff parameters were used for the protein and POPE lipids. The particle mesh Ewald method was used, and the direct space cutoff distance was set to 12 Å. The program package that we used for the MD simulations was Amber 8 (23).

Parameter of Cys-SHg$^+$ residue

We have developed force field and parameter for mercury to be used in our MD simulation. To develop force field and parameters, we referred to a previous report by Fuchs et al. (24). Table 1 shows force field and parameters of Cys-SHg$^+$. The geometries of the Cys-SHg$^+$ residue were optimized at the Hartree-Fock level, using the LANL2D and 6-31G** basis set for mercury and the other atoms, respectively, and Gaussian03 (25). Table 1 shows van der Waals forces and bonded parameters of Cys-SHg$^+$. The RESP charges were calculated and assigned using the ANTECHAMBER module from Amber 8 (23) (see Fig. S1 in the Supporting Material).

The free energy profile using umbrella sampling

We calculated the free energy profiles for water transport through AQP1 using the umbrella sampling technique (26). At this time, we used the water transport path for Free AQP1 as the reaction coordinate. In the umbrella sampling, a biasing potential (V, given by Eq. 1) was added to the Hamiltonian of the system, and the biased distributions were collected.

$$V = \frac{1}{2}k(x - x_0)^2, \tag{1}$$

where x_0 is a reference value (a distance from a dummy atom to a water molecule) on the reaction coordinate. The dummy atom was placed 30 Å below the center of the ar/R region, along the z axis. The umbrella potential k was set to be 0.01 (kcal/mol Å) and a gap distance of 1.0 Å was used for all sampling simulations. We carried out a 50 ps MD simulation for each sampling window. The biased distributions obtained using the umbrella sampling simulations were unbiased using the weighted histogram analysis method (WHAM) (27–29).

Diffusion permeability

The diffusion permeability was analyzed during the last 10 ns of the MD trajectory for each system. The diffusion permeability was calculated using Eq. 2 (21):

$$p_d = \frac{V_W}{N_A}q_0 = v_W q_0, \tag{2}$$

TABLE 1 Parameter of Cys-SHg$^+$

van der Waals parameters				
Atom	R (Å)	∈ (kcal/mol)		
Hg(GG)	1.60	1.0		
Bond distance	K bond	R bond (Å)		
SH-GG	600	2.350		
Bond angle	Kθ	Equilibrium value (°)		
CT-SH-GG	45.0	103.0		
	Dihedral angle	Torsions (n)	Barrier magnitude	Periodicity
	(IDIVF)	(PK)	(PHASE)	(PN)
CT-CT-SH-GG	3	0.75	0.0	3.
H1-CT-SH-GG	3	0.75	0.0	3.

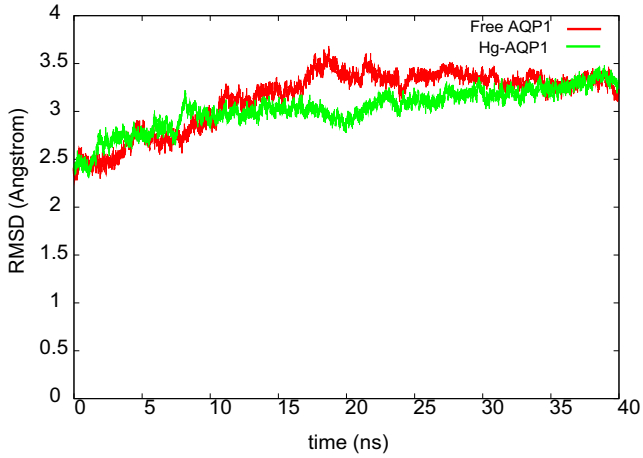

FIGURE 2 RMSD curves indicate the conformations of Free AQP1 (*green line*) and Hg-AQP1 (*red line*).

where p_d (cm^3/s/pore) is the diffusion permeability coefficient per pore, V_W is the molar volume of the solvent, N_A is Avogadro's number, q_0 is the unidirectional permeation rate, and v_w is the volume of a single solvent molecule. q_0 was calculated by counting the number of water molecules passing from one side of the channel to the other per unit time. The pore region was chosen to be the narrow central section of the channel (between Arg^{197} and His^{182} and between Val^{155} and His^{76}). The pore is 20 Å in length, through which the water molecules pass in single file or nearly in single file.

RESULTS

We carried out two 40 ns MD simulations of both Free AQP1 and Hg-AQP1. First, we observed the root mean-square deviations (RMSDs) of main chain from the x-ray crystal structure. The main chain RMSD curves for the entire structures of both Free AQP1 and Hg-AQP1 are shown in Fig. 2. The conformations of Free AQP1 and Hg-AQP1 are stable after 30 ns (i.e., the last 10 ns), and these RMSD values converge to ~3.5 Å. It is clear that the structural differences from the crystal structure are derived, not from the relative position changes of the four monomers, but from the conformational changes within each monomer because the RMSD values of each monomer are ~3.2–3.3 Å. In addition, from the x-ray structure, the main chain RMSD for the secondary structure (H1: 3–28; H2: 38–58; HB: 67–78; H3: 82–106; H4: 126–149; H5: 160–174; HE: 183–195; H6: 20–223) of the Hg-AQP1 monomer and that of Free AQP1 are ~1.2 Å, respectively (not shown). These results indicate that the secondary structures of Free AQP1 and Hg-AQP1 resemble each other and remain stable, but some other parts of the molecule (i.e., the loop regions) are flexible. The stability of the secondary structures and the flexibility of loop regions can also be seen by visual inspection of the final MD structures of both Free AQP1 and Hg-AQP1 (Fig. 3). We therefore conclude that the last 10 ns of the MD trajectories of Free AQP1 and Hg-AQP1 had been fully equilibrated.

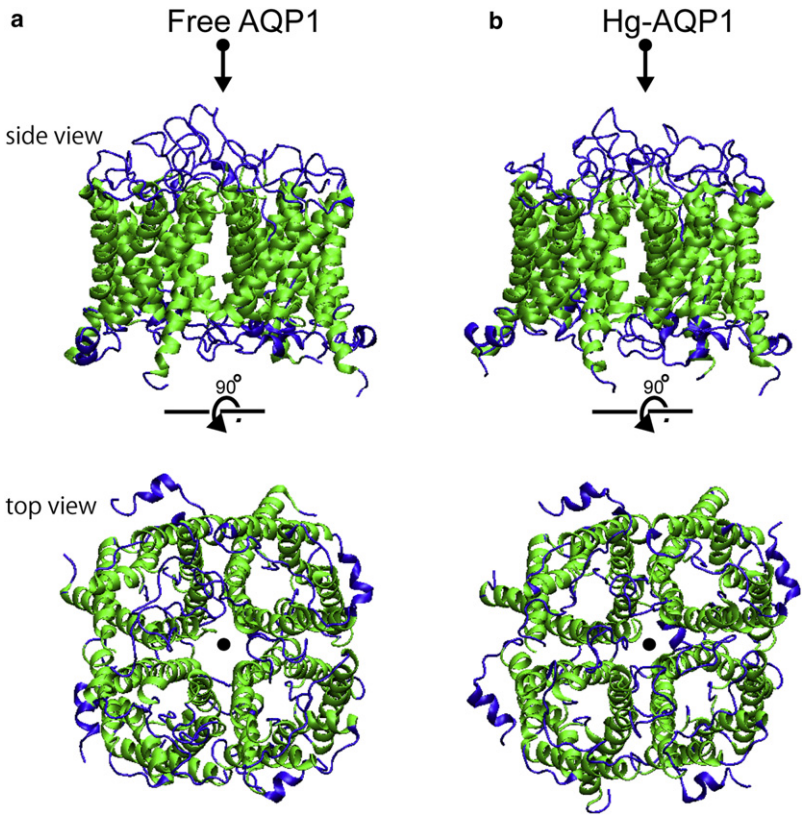

FIGURE 3 Snapshots (40 ns) of (*a*) Free AQP1 and (*b*) Hg-AQP1. The green ribbons and blue lines show the helices (see Fig. 1 *b*) and other structures, respectively.

To check whether the binding of mercury to Cys^{191} had influenced the permeation of water in AQP1, we obtained the unidirectional permeation rate of water by counting the number of events in which a water molecule completely passed through the AQP1 channel pore over the last 10 ns of the simulation. The water-conducting pore is defined as the space between His^{182}–Arg^{197} and His^{76}–Val^{155}. Water permeated Free AQP1 23 times and Hg-AQP1 0 times (Table 2), indicating that mercury binding has a strong influence on the permeation of water through AQP1.

Fig. 4 shows the radius of the water pore along water permeation route. The trajectory of the radius of the pore in Free AQP1 resembled that of the x-ray structure, but we observed that Hg-AQP1 had a slightly different trajectory from the x-ray or Free AQP1 structures. The narrowest region of the pore is observed at the ar/R region, and contains Cys^{191} both in Free AQP1 and in Hg-AQP1. At this region, the radius of the pore of Hg-AQP1 is smaller than that of Free AQP1, indicating that the binding of mercury induces conformational changes at the ar/R region, including at Cys^{191}. We therefore focused on the conformational changes near Cys^{191} that accompany the binding of mercury. A comparison of the conformation at the ar/R region between Free AQP1 and Hg-AQP1 is shown in Fig. 5. In Free AQP1, water molecules can access the space between Arg^{197} and His^{182} and form hydrogen bonds with amino acids, isolated from other water molecules. The main-chain carbonyl oxygen atoms of Gly^{190}, Cys^{191}, and Gly^{192} form a line, and are oriented inside the water pore. At this time, Glu^{144} contributes to the maintenance of the conformation of Gly^{192} and Ile^{193} by forming several hydrogen bonds (Fig. 5 *a*). In Hg-AQP1, it is obvious that the space between Arg^{197} and His^{182} has become too small for water to pass through (Fig. 4 and Fig. 5 *b*). Moreover, the carbonyl oxygen atoms of Gly^{190} and Gly^{192} did not orient inside the water pore, thereby not forming a line. Glu^{144} formed hydrogen bonds with Gly^{192}, but not with Ile^{193} (Fig. 5 *b*). The positive charges of mercury and the side chain of Arg197 repelled each other. As a result, the side chain (-SHg^{+}) of Cys^{191}-SHg^{+} residue was oriented toward the outside of the water pore. This repulsion induces the collapse of the orientation of the backbone carbonyl oxygen of Gly^{190}, Cys^{191}, and Gly^{192} and breaks the hydrogen bonds between Glu^{144} and Ile^{193}. Taking these results together, we suggest that mercury binding induces the collapse of orientations of the key amino acid residues near the ar/R region, which may produce a high-energy barrier that blocks the passage of water through the pore.

TABLE 2 Comparison of water permeation between Free AQP1 and Hg-AQP1

Time	Free AQP1 (10 ns)	Hg-AQP1(C191) (10 ns)	Hg-AQP1(C154) (5 ns)
Permeation events (*n*)	23	0	14
Water permeation rate (water(s)/ns/monomer)	0.288	—	0.350

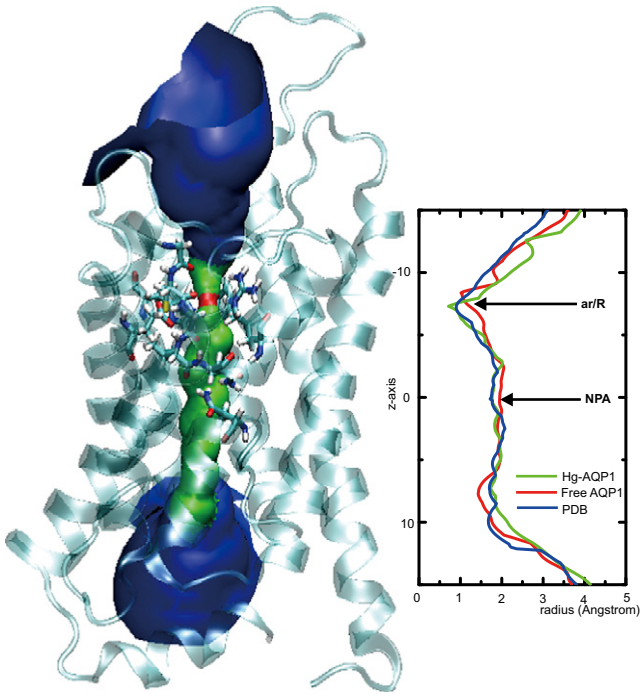

FIGURE 4 The averaged radius (*r*) of the pore region (*left*) and a structural image of the position of the water pore (*right*). The figure also shows the radii of the water pores in Free AQP1 (*red line*), Hg-AQP1 (*green line*), and the PDB structure (*blue line*). The vertical axis indicates the distances toward the cytoplasm (+) or toward the extra-cellular region (−) from the center of the NPA region. The abscissa axis indicates the channel radii (*r*). The radii of the water pores were determined using the program HOLE2 (40).

We then investigated the effects of the collapse of the ar/R conformation on the permeation of water by calculating the free energy profiles. The potential mean forces (PMFs) for the permeation of a water molecule are shown in Fig. 6. The highest energy barriers are found at the ar/R region in both in Free AQP1 and Hg-AQP1, although the energy barrier for Hg-AQP1 is much higher than that of Free AQP1. Taken together, these results demonstrate that mercury binding causes conformational changes at the ar/R region (including Cys^{191}), leading to the inhibition of water permeation.

We next examine whether the binding of mercury to other cysteine residues can induce similar conformational changes. We constructed a Cys^{154}-SHg^{+} (Hg-AQP1 (C154)) structure using the same conditions as for Hg-AQP1 (C191) and carried out a 35-ns MD simulation. Note that Cys^{154} in bovine AQP1 is corresponding to Cys^{152} in human AQP1 and that C152S mutant of human AQP1 is inhibited by mercury as is wild-type AQP1 (10). The water permeability in Hg-AQP1 (C154) and in Free AQP1 is 0.350 and 0.288 water(s)/ns/monomer, respectively (Table 2). Our results from the MD simulation are, therefore, consistent with the previous experimental data by Preston et al. (10). Furthermore, the orientation at the ar/R region of Hg-AQP1 (C154) was not altered (data not shown), suggesting that the conformational changes seen in Hg-AQP1 (C191) is specific to Cys^{191} residue.

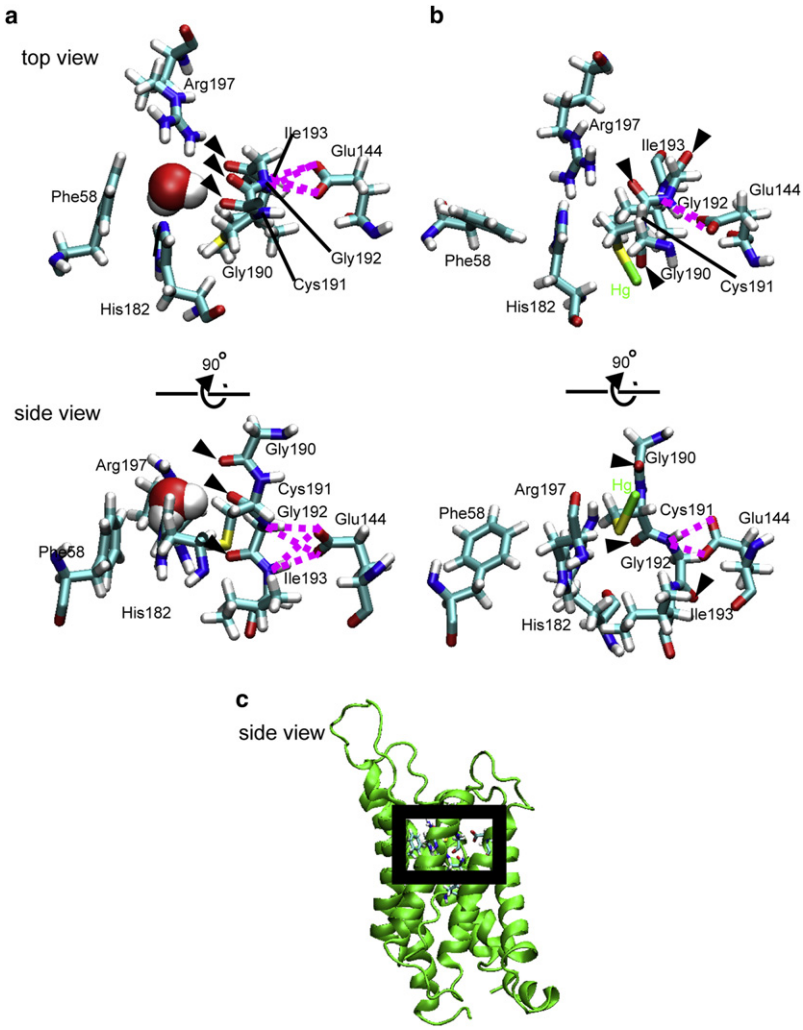

FIGURE 5 The orientation at the ar/R region, depicted from the top (*upper*) and a side (*lower*) view. Phe^{58}, Glu^{144}, His^{182}, Gly^{190}, Cys^{191}, Gly^{191}, Ile^{193}, and Arg^{197} residues are drawn using stick models. (*a*) The orientation at the ar/R region in Free AQP1. Glu^{144} has formed 4 hydrogen bonds with both Gly^{192} and Ile^{193} (*pink dotted lines*). These hydrogen bonds maintain the position of the backbone oxygen atoms of Gly^{192} and Ile^{193} in a line. (*b*) The orientation at the ar/R region in Hg-AQP1. Glu^{144} has formed two hydrogen bonds, only with Gly^{192} (*pink dotted lines*). These hydrogen bonds are not sufficient to maintain the position of the backbone oxygen atoms Gly^{192} and Ile^{193} in a line. As a result, the backbone oxygen atoms of Gly^{190} and Ile^{193} are not directed toward the water pore. Mercury did not plug the water pore. Black arrows in *a* and *b* indicate the backbone oxygen atoms of Gly^{190}, Cys^{191}, and Gly^{192}, respectively. (*c*) The side view of an AQP1 monomer. The rectangular box indicates the position of the ar/R region shown above.

DISCUSSION

Comparison of the water permeability results with previous simulations and experimental data.

Our MD-derived, average unidirectional permeation rate was calculated to be 0.288 waters/ns/AQP1 monomer. This is in good agreement with the experimental data and previous MD simulations of bovine AQP1 (30,31). A previous MD study by Mamonov et al. (30) reported that the p_d of water molecules is 0.85×10^{-14} cm^3/s/pore, as determined using equilibrium MD simulations. From our MD simulations using Eq. 2, we found p_d of Free AQP1 to be 0.86×10^{-14} cm^3/s/pore, which is consistent with the previous MD simulations. The experimental value of the osmotic water permeability coefficient (p_f) is ~4–10 $\times$ 10^{-14} cm^3/s (32–35). p_f values obtained by MD simulation of AQP1 have been reported at ~7–10 $\times$ 10^{-14} cm^3/s (21). Approximately eight water molecules exist in the pore region that we have chosen. Finkelstein proposed for single-file water transport, that the predicted p_f/p_d ratio is N or $N + 1$ (36). We estimated p_f, which is also in good agreement with previous reports (21,30–36).

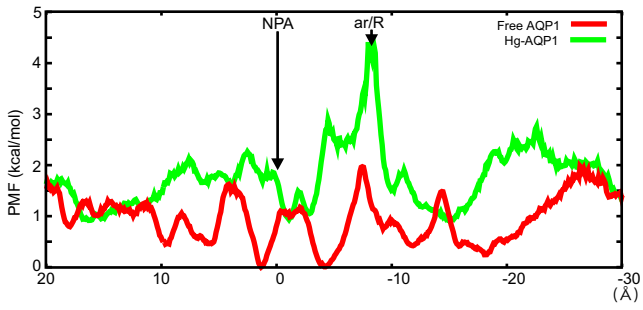

FIGURE 6 The PMF of Free AQP1 (*red*) and Hg-AQP1 (*green*). An energy barrier exists at the ar/R region in both structures, but the energy barrier of Hg-AQP1 is higher than that of Free AQP1. The vertical axis indicates the PMF value. The abscissa axis indicates distances toward the cytoplasm (+) or toward the extracellular region (−) from the NPA region.

It is thought that cysteine residues, which exist along the water pore of AQP1, are sensitive to mercury. There are four cysteine residues in human AQP1: C87, C102, C152, and C189. Preston et al. (10) have identified Cys^{189} as a mercurial binding site to inhibit the water permeability by

site-directed mutagenesis experiments. We also constructed the C152S, C189S, and C152S/C189S double mutants of human AQP1. Note that Cys^{152} and C189 of human AQP1 correspond to Cys154 and Cys^{191} of bovine AQP1, respectively. The osmotic water permeability of these mutants was measured in the presence and absence of 300 μM $HgCl_2$ using the oocyte swelling assay (data not shown). The water permeability of C152S was decreased by mercury (as wild-type AQP1 is). In contrast, the C189S or C152S/C189S double mutant was not inhibited by mercury, indicating that Cys^{189} (but not Cys^{152}) is the target residue for mercurial inhibition of human AQP1. These results indicate that Cys^{189} of human AQP1, which corresponds to Cys^{191} in bovine AQP1, is a mercury sensitive residue. In our MD simulation, the water permeation rates of Cys-AQP1 (0.350 waters/ns/monomer) and Free AQP1 (0.288 waters/ns/monomer) were similar (Table 2). Moreover, the orientation at the ar/R region of Hg-AQP1 (C154) was not altered. These results indicate that our MD simulations adequately reproduced the experimental data; mercury binding at Cys^{154} does not influence the water permeability of AQP1.

The mechanisms of mercurial inhibition

There are two hypotheses for the mechanism of inhibition of AQP1 by mercury; the first is simple occlusion of the channel pore by mercury. The second is that the pore is collapsed by conformational changes at the ar/R region, where the mercury-sensitive cysteine residue is located. Our MD simulation supports the second one. First, PMFs showed that the energy barrier for Hg-AQP1 is much higher than that of Free AQP1 at the ar/R region. Second, our MD simulations show that mercury binding induces a collapse of the orientation of amino acid residues at the ar/R region and the constriction of the space between Arg^{197} and His^{182} (Fig. 5 *b*). In Free AQP1, four hydrogen bonds were observed between Glu^{144}–Gly^{192} and between Glu^{144}–Ile193 during the simulations (Fig. 5 *a*). However, in Hg-AQP1, only two hydrogen bonds were kept, between Glu^{144}–Gly^{192}, and no line was formed by the three residues (Fig. 5 *b*). These hydrogen bonds play an important role in forming the line of the three residues, Gly^{190}, Cys^{191}, and Gly^{192}. The line acts to guide the movement of water from the ar/R region to the NPA region. Fig. 7 shows snapshots of all water molecules in the pore region in Free AQP1 and Hg-AQP1 along with relevant residues. In Free AQP1, single file orientation of water molecules was observed (Fig. 7 *a*). And water molecules around ar/R region and NPA motif formed hydrogen bonds with side chains of Arg^{197} and His^{182} and backbone oxygen atom of Cys^{191} and two asparagine residues (Asn^{78} and Asn^{194}) of NPA motif, respectively. In Hg-AQP1, however, the space at ar/R

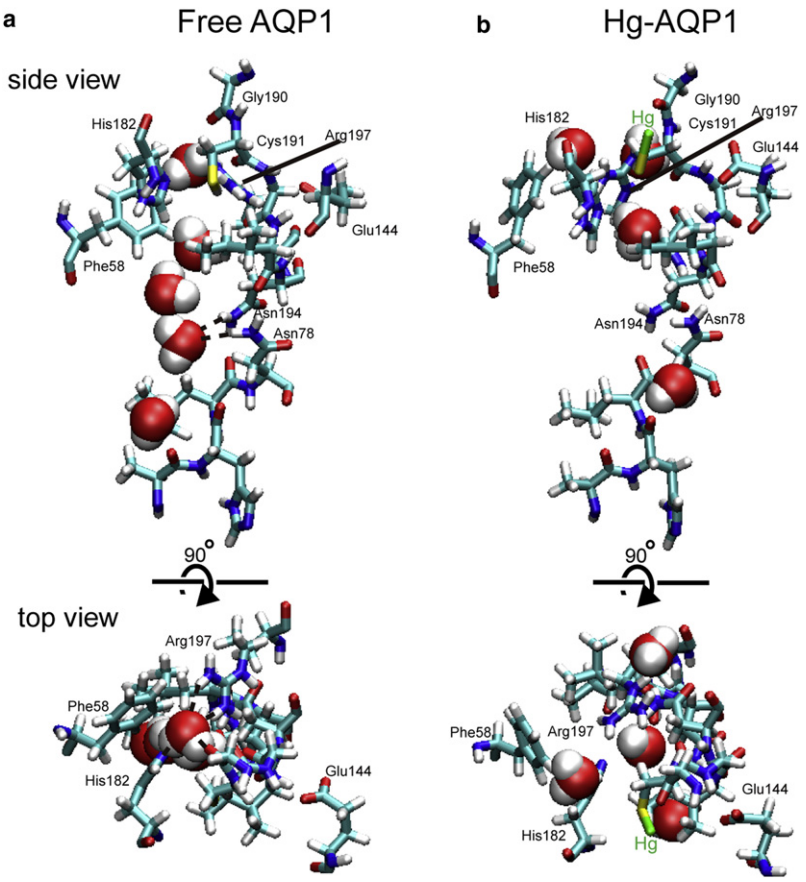

FIGURE 7 Snapshots of water molecules in the water pore depicted from a side (*upper*) and top (*lower*) view. Phe^{58}, Ala^{75}, His^{76}, Leu^{77}, Asn^{78}, Glu^{144}, His^{182}, Gly^{190}, Cys^{191}, Gly^{191}, Ile^{193}, and Arg^{197} residues are drawn using stick models and water molecules are drawn van der Waals models. (*a*) The orientation of water molecules in water pore of Free AQP1. Single file orientation of water molecules was observed. Simultaneously, water molecules around ar/R region and NPA motif formed hydrogen bonds with side chains of Arg^{197} and His^{182} and backbone oxygen atom of Cys^{191} and two Asn residues of NPA motif, respectively. (*b*) The orientation of water molecules in water pore of Hg-AQP1. The space at ar/R region was too narrow to conduct water molecules. Furthermore, water molecules were disordered and not formed hydrogen bonds with any amino acid residues.

region was too small for water to be permeated (Fig. 7 *b*). Furthermore, water molecules were disordered and not formed hydrogen bonds with protein because the line formed by the three residues was collapsed. Our results indicate that permeation of water is inhibited when the orientation of the backbone oxygen atoms into a line is collapsed by mercury binding to Cys^{191}. Therefore, we propose that mercury inhibits the permeation of water through AQP1 by inducing conformational changes at the ar/R region rather than simply plugging the pore.

On the other hand, our MD simulation can not exclude the first hypothesis that is the simple occlusion of the pore by mercury. Indeed, during MD simulation of Hg-AQP1 (C191), there were some moments that mercury atom exists in the pore. Recently, Savage and Stroud (37) designed a mutant of T183C-AQPZ and obtained a structure with two mercury sites (both binding to Cys^{183}) by x-ray crystallography; the one mercury is located inside the pore that can occlude the pore for water conduction, the other mercury is found buried in an interstitial cavity, supporting the occlusion model. The mechanism of mercurial inhibition of AQPZ might be different from that of AQP1 because the water permeability of WT-AQPZ is also inhibited by $HgCl_2$ despite no cysteine residue at the ar/R region and because the basal water permeability of T183C-AQPZ is slightly lower than that of WT-AQPZ. Interestingly, they found the one mercury is interacting with Glu^{138} (corresponding to Glu^{144} in bovine AQP1) that is important for maintaining the orientation of the backbone carbonyl oxygen of Gly^{190}, Cys^{191}, and Gly^{192} (Fig. 5 and Kozono et al. (38)). This may imply that a similar conformational change can be occurred in T183C-AQPZ. It is, therefore interesting to carry out MD simulation of T183-AQPZ with mercury in the future.

SUPPORTING MATERIAL

One figure is available at http://www.biophysj.org/biophysj/supplemental/S0006-3495(10)00011-1.

We thank Dr. Atsushi Suenaga for worthwhile advice in this study. This study was conducted by using the resource of 8-dual-dual core Opteron processor Beowulf Cluster (Takeru64 Opt Cluster, Tsukuba, Japan).

This work was supported by leading project for Bio-simulation from NEXT (M.S., M.Y.), the Japan New Energy and Industrial Technology Development Organization (NEDO) (M.Y.), the Next-Generation Integrated Simulation of Living Matter (M.S., M.Y.), Grant-in-Aid for Young Scientists (B) from Japan Society for the Promotion of Science (JSPS) (Y.H.), and Keio Gijuku Academic Development Funds (Y.H.).

REFERENCES

1. Agre, P., L. S. King, …, S. Nielsen. 2002. Aquaporin water channels—from atomic structure to clinical medicine. *J. Physiol.* 542:3–16.
2. Itoh, T., T. Rai, …, K. Ishibashi. 2005. Identification of a novel aquaporin, AQP12, expressed in pancreatic acinar cells. *Biochem. Biophys. Res. Commun.* 330:832–838.
3. de Groot, B. L., T. Frigato, …, H. Grubmüller. 2003. The mechanism of proton exclusion in the aquaporin-1 water channel. *J. Mol. Biol.* 333:279–293.
4. Chen, H., Y. Wu, and G. A. Voth. 2006. Origins of proton transport behavior from selectivity domain mutations of the aquaporin-1 channel. *Biophys. J.* 90:L73–L75.
5. Herrera, M., N. J. Hong, and J. L. Garvin. 2006. Aquaporin-1 transports NO across cell membranes. *Hypertension.* 48:157–164.
6. Holm, L. M., T. P. Jahn, …, T. Zeuthen. 2005. NH^3 and NH^{4+} permeability in aquaporin-expressing Xenopus oocytes. *Pflugers Arch.* 450:415–428.
7. Ivanov, I. I., A. V. Loktyushkin, …, A. B. Rubin. 2007. Oxygen channels of erythrocyte membrane. *Dokl. Biochem. Biophys.* 414:137–140.
8. Nakhoul, N. L., B. A. Davis, …, W. F. Boron. 1998. Effect of expressing the water channel aquaporin-1 on the CO_2 permeability of *Xenopus* oocytes. *Am. J. Physiol. Cell Physiol.* 43:C543–C548.
9. Fu, D., A. Libson, …, R. M. Stroud. 2000. Structure of a glycerol-conducting channel and the basis for its selectivity. *Science.* 290:481–486.
10. Preston, G. M., J. S. Jung, …, P. Agre. 1993. The mercury-sensitive residue at cysteine 189 in the CHIP28 water channel. *J. Biol. Chem.* 268:17–20.
11. Zhang, R., A. N. van Hoek, …, A. S. Verkman. 1993. A point mutation at cysteine 189 blocks the water permeability of rat kidney water channel CHIP28k. *Biochemistry.* 32:2938–2941.
12. Hasegawa, H., S. C. Lian, …, A. S. Verkman. 1994. Extrarenal tissue distribution of CHIP28 water channels by in situ hybridization and antibody staining. *Am. J. Physiol.* 266:C893–C903.
13. Burykin, A., and A. Warshel. 2003. What really prevents proton transport through aquaporin? Charge self-energy versus proton wire proposals. *Biophys. J.* 85:3696–3706.
14. Burykin, A., and A. Warshel. 2004. On the origin of the electrostatic barrier for proton transport in aquaporin. *FEBS Lett.* 570:41–46.
15. de Groot, B. L., and H. Grubmüller. 2001. Water permeation across biological membranes: mechanism and dynamics of aquaporin-1 and GlpF. *Science.* 294:2353–2357.
16. de Groot, B. L., and H. Grubmüller. 2005. The dynamics and energetics of water permeation and proton exclusion in aquaporins. *Curr. Opin. Struct. Biol.* 15:176–183.
17. Hashido, M., M. Ikeguchi, and A. Kidera. 2005. Comparative simulations of aquaporin family: AQP1, AQPZ, AQP0, and GlpF. *FEBS Lett.* 579:5549–5552.
18. Tajkhorshid, E., P. Nollert, …, K. Schulten. 2002. Control of the selectivity of the aquaporin water channel family by global orientational tuning. *Science.* 296:525–530.
19. Wang, Y., J. Cohen, …, E. Tajkhorshid. 2007. Exploring gas permeability of cellular membranes and membrane channels with molecular dynamics. *J. Struct. Biol.* 157:534–544.
20. Zhu, F., E. Tajkhorshid, and K. Schulten. 2002. Pressure-induced water transport in membrane channels studied by molecular dynamics. *Biophys. J.* 83:154–160.
21. Zhu, F., E. Tajkhorshid, and K. Schulten. 2004. Theory and simulation of water permeation in aquaporin-1. *Biophys. J.* 86:50–57.
22. Sui, H., B. G. Han, …, B. K. Jap. 2001. Structural basis of water-specific transport through the AQP1 water channel. *Nature.* 414: 872–878.
23. Case, D. A., Y. A. Darden, …, P. A. Kollman. 2004. AMBER 8. University of California, San Francisco, CA.
24. Fuchs, J. F., H. Nedev, …, S. Crouzy. 2006. New model potentials for sulfur-copper(I) and sulfur-mercury(II) interactions in proteins: from ab initio to molecular dynamics. *J. Comput. Chem.* 27:837–856.
25. Frisch, M. J., G. W. Trucks, ..., J. A. Pople. 2004. Gaussian 03. Gaussian, Wallingford CT.
26. Torrie, G. M., and J. P. Valleau. 1977. Non-physical sampling distributions in Monte-Carlo free-energy estimation—umbrella sampling. *J. Comput. Phys.* 23:187–199.

27. Boczko, E. M., and C. L. Brooks. 1993. Constant-temperature free-energy surfaces for physical and chemical processes. *J. Phys. Chem.* 97:4509–4513.

28. Kumar, S., D. Bouzida, …, J. M. Rosenberg. 1992. The weighted histogram analysis method for free-energy calculations on biomolecules. 1. The method. *J. Comput. Chem.* 13:1011–1021.

29. Roux, B. 1995. The calculation of the potential of mean force using computer-simulations. *Comput. Phys. Commun.* 91:275–282.

30. Mamonov, A. B., R. D. Coalson, …, J. C. Mathai. 2007. Water and deuterium oxide permeability through aquaporin 1: MD predictions and experimental verification. *J. Gen. Physiol.* 130:111–116.

31. Vidossich, P., M. Cascella, and P. Carloni. 2004. Dynamics and energetics of water permeation through the aquaporin channel. *Proteins.* 55:924–931.

32. Walz, T., B. L. Smith, …, P. Agre. 1994. Biologically active two-dimensional crystals of aquaporin CHIP. *J. Biol. Chem.* 269:1583–1586.

33. Yang, M., B. Yordanov, …, S. Huo. 2006. The sequence-dependent unfolding pathway plays a critical role in the amyloidogenicity of transthyretin. *Biochemistry.* 45:11992–12002.

34. Zeidel, M. L., S. V. Ambudkar, …, P. Agre. 1992. Reconstitution of functional water channels in liposomes containing purified red cell CHIP28 protein. *Biochemistry.* 31:7436–7440.

35. Zeidel, M. L., S. Nielsen, …, P. Agre. 1994. Ultrastructure, pharmacologic inhibition, and transport selectivity of aquaporin channel-forming integral protein in proteoliposomes. *Biochemistry.* 33:1606–1615.

36. Finkelstein, A. 1987. Water Movement Through Lipid Bilayers, Pores, and Plasma Membranes. John Wiley & Sons, New York, NY.

37. Savage, D. F., and R. M. Stroud. 2007. Structural basis of aquaporin inhibition by mercury. *J. Mol. Biol.* 368:607–617.

38. Kozono, D., M. Yasui, …, P. Agre. 2002. Aquaporin water channels: atomic structure molecular dynamics meet clinical medicine. *J. Clin. Invest.* 109:1395–1399.

39. Humphrey, W., A. Dalke, and K. Schulten. 1996. VMD: visual molecular dynamics. *J. Mol. Graph.* 14, 33–38, 27–28.

40. Smart, O. S., J. G. Neduvelil, …, M. S. P. Sansom. 1996. HOLE: a program for the analysis of the pore dimensions of ion channel structural models. *J. Mol. Graph. Model.* 14:354–360.